

Elemental bio-imaging: *In situ* analysis of
trace elements in tissue by laser ablation –
inductively coupled plasma – mass
spectrometry

by

Dominic Hare

A thesis submitted for the
Degree of Doctor of Philosophy (Science)

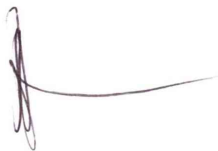
University of Technology, Sydney

January 2009

Certificate of authorship and originality

I certify that the work in this thesis has not previously been submitted for a degree nor has it been submitted as part of the requirements for a degree except as fully acknowledged within the text.

I also certify that the thesis has been written by me. Any help that I have received in my research work and the preparation of the thesis itself has been acknowledged. In addition, I certify that all the information sources and literature used are indicated in the thesis.



Dominic Hare

26 January 2009



This thesis is dedicated to my godmother Mary McFall, with the hope that it may add to the global effort aiming to help treat the millions suffering from Parkinson's disease, just like her.

Acknowledgements

There are many people who deserve recognition and thanks for their involvement in this project, and after three years I think I'm allowed to indulge.

Firstly, Dr Philip Doble, who spent many an hour ensuring that this project would have the impact it deserves in the right fields. His knowledge of analytical chemistry and experiences in both academia and industry have been a constant source of inspiration since I first stepped foot in his lecture theatre. Without Phil's constant support, advocacy and the ability to push me to achieve my absolute best this project would never have bore the fruit it ultimately did, and for that I am truly grateful.

Dr Brian Reedy, who's significant input not only during the initial phase of this project, but for the full three years over which it was carried out, also bears much responsibility for the work that was produced. Associate Professor Michael Dawson, who as both the head of department and as my co-supervisor is one of the best friends a student can have in the modern university climate. Dr Val Spikmans, with whom I commenced this project, helped get the ideas off the ground.

Many thanks also go to my fellow ICP-MS using research students, Christine Austin and David Bishop, who are both another constant source of ideas and inspiration. Tristan Rawling deserves special thanks for constantly belittling my choice of vocation, which only served to make me more determined to prove him wrong. How's that light bulb coming along, Tristan? Thanks also to Alison Beavis for her support since first year.

Per Andren and Per Sveniggson from Uppsala University and the Karolinska Institute in Sweden also deserve thanks for providing my initial samples for method development experiments.

The project relied heavily on the support of David Finkelstein, Simon Wilkins, Jessica George, Ashley Bush and Robert Cherny from the Mental Health Research Institute of Victoria. Their incredible assistance in providing a fantastic model to test the method I developed, and for

answering innumerable questions about areas of biology that were once foreign to me was invaluable. I believe they are some of the finest scientists in Australia.

I also wish to thank Richard Scolyer and John Thompson of the Sydney Melanoma Unit for providing samples and support.

Rosalba Zumbo, Michael Rodriguez, Fawaz Zouabi, Patrick Moody and the staff of the histology laboratory from the Department of Forensic Medicine, Glebe gave much assistance with all things histological. They also provided a welcome refuge when the time needed, and are all very close friends.

Special credit goes to Fred Fryer of Agilent Technologies Australia, whose years of ICP-MS experience make him one of the most valued people to know in this industry. He's also a pretty amazing guy too.

To my close friends I must also give thanks for their support over the past 7 years. I wasn't going to name them, but, well, I can, so to Jack Davison, Peter McMaster, Anna Coleman, Jordy Bertram, Ryan Shaw, Klayton Brisby, James Tannock, Shannon Loughlin and Sara Griffin I give many, many thanks.

Both my immediate and extended family also gave much love and support through the whole process, and I could not have done it without them. Mum and dad, I promise I'll call more often from now on. To Kyom, Maith and Kerry Behrend, as well as Jenna Hall, thank you for accepting me into your family.

To Tony Coleman and Wesley Pentz for providing the Hospital Records and Mad Decent Worldwide Radio podcasts for providing much needed sanity and tuneage during the write-up phase.

And finally, to my wife, Zeah Behrend, I give the most important acknowledgement. Zeah's love, support, patience and understanding throughout what has been one of the most tumultuous times of my life is just one of the reasons I love her so much. And it's for all the other reasons that I'll keep doing what I'm doing now.

Table of contents

Certificate of authorship and originality.....	ii
Acknowledgements.....	iv
Table of contents.....	vi
List of figures.....	ix
List of tables.....	xvi
List of publications.....	xviii
Abstract.....	xx
1 Introduction.....	1
1.1 Trace elements in health and disease.....	2
1.1.1 Metallomics and metal-binding proteins.....	6
1.1.1.1 Definitions of metallomics.....	7
1.1.1.2 Analytical techniques for metallomics.....	9
1.1.1.3 Metal binding to proteins and peptides.....	10
1.1.2 Melanoma.....	12
1.1.2.1 Causes.....	12
1.1.2.2 Trace elements and melanoma.....	13
1.1.2.3 Sentinel lymph nodes.....	15
1.1.2.4 Histopathology.....	17
1.1.2.5 Chemical imaging of melanoma.....	19
1.1.3 Metals and neurodegenerative disorders.....	22
1.1.3.1 Neurotoxicity of trace heavy metal exposure.....	23
1.1.3.2 Metal transport and homeostasis.....	25
1.1.3.3 Redox properties of metals and the reactive oxygen species.....	28
1.1.3.4 Alzheimer's disease.....	31
1.1.4 Parkinson's disease.....	34
1.1.4.1 Causes.....	36
1.1.4.2 Metal-mediated protein aggregation.....	39
1.1.4.3 Brain iron.....	40
1.1.4.4 Metal chelators as therapeutics.....	42
1.1.4.5 Animal models for Parkinson's disease.....	44
1.2 Laser ablation-inductively coupled plasma-mass spectrometry.....	47
1.2.1 Inductively coupled plasma – mass spectrometry.....	47
1.2.1.1 Inductively coupled plasma as an ionisation source.....	49
1.2.1.2 Interface.....	52
1.2.1.3 Ion focusing.....	53
1.2.1.4 Mass analysers.....	54
1.2.1.5 Interferences.....	57
1.2.2 Laser ablation.....	61
1.2.2.1 Laser principles and emission sources.....	63
1.2.2.2 Crater formation and elemental fractionation.....	67
1.2.2.3 Ablation chamber design.....	69
1.2.2.4 Future directions of laser ablation.....	71
1.2.3 Challenges and limitations of LA-ICP-MS.....	72
1.2.3.1 Quantification and calibration strategies.....	72
1.2.3.2 Internal standardisation.....	73
1.2.3.3 Matrix-based interferences.....	75

1.2.3.4	Helium vs. argon	76
1.3	Imaging.....	77
1.3.1	Instrumentation	79
1.3.2	Data treatment	79
1.3.3	Human tissue	80
1.3.4	Animal models	85
1.3.5	Other matrices	89
1.3.6	Quantification strategies for imaging.....	90
1.4	Aims and scope	95
2	Experimental.....	96
2.1	Instrumentation.....	96
2.1.1	Inductively coupled plasma – mass spectrometer	96
2.1.2	Laser ablation unit	97
2.1.3	Solution ICP-MS operational parameters	98
2.1.4	LA-ICP-MS operational parameters.....	100
2.2	Data acquisition and processing.....	101
2.2.1	Experimental set-up	101
2.2.2	Image construction	102
2.2.3	Macros and Visual Basic	105
2.3	External calibration	105
2.3.1	Tissue homogenisation.....	106
2.3.2	Microwave assisted digestion.....	107
2.3.3	Solution ICP-MS analysis	108
2.3.4	Tissue sectioning.....	109
2.3.5	Data acquisition	109
2.3.6	Linear regression	110
2.4	Interference experiments	111
2.4.1	Matrix-based interferences (glass substrate)	112
2.4.2	Matrix-based interferences (tissue substrate)	113
2.5	Melanoma samples	114
2.6	Parkinsonism animal models	115
2.6.1	6-OHDA lesioned rats (Karolinska Institutet).....	115
2.6.2	6-OHDA lesioned mice (MHRIV)	117
2.6.3	Neonatal Fe fed.....	118
2.6.3.1	Clioquinol treated animals	119
2.6.3.2	L-DOPA treated animals	119
2.6.4	Brain regions	120
3	Development of elemental bio-imaging procedure.....	121
3.1	Spot ablation.....	121
3.1.1	Experimental parameters	121
3.1.2	Results	124
3.2	Line ablation.....	131
3.2.1	Experimental parameters	131
3.2.2	Results	132
3.3	Data treatment	133
3.3.1	SigmaPlot images.....	133
3.3.2	ENVI images and Excel VBA Macros	135
3.4	Evaluation of Octopole Reaction System.....	136
3.5	Considerations	142
3.5.1	Spot vs. lines ablation.....	142

3.5.2	Runtime	146
3.5.3	Laser power and energy output	146
3.5.4	Signal normalisation	152
3.5.5	Gas quality	156
3.5.6	Contamination/cutting artefact	159
3.5.7	Mass spectrometer parameters	161
3.6	Conclusions	162
4	Evaluation of matrix-based interferences in LA-ICP-MS	164
4.1	Method	164
4.2	Droplet ablation (glass substrate)	165
4.2.1	Natural isotopic abundance ratios	167
4.3	Droplet ablation (tissue substrate)	168
4.3.1	Natural isotopic abundance ratios	172
4.4	Discussion	172
4.5	Conclusions	174
5	Application of elemental bio-imaging to melanoma in lymph node biopsies.....	176
5.1	Histopathology	178
5.2	Images	178
5.3	Tumour boundaries	184
5.4	Small size tumour analysis	185
5.5	Three-dimensional surface models	186
5.6	Sample throughput considerations	189
5.7	Conclusions	190
6	Analysis of matrix-matched tissue standards	191
6.1	Calibration data	191
6.2	Analysis of digests	193
6.3	Discussion of results	194
6.4	Conclusions	196
7	Application of elemental bio-imaging to iron fed neonate rodents	197
7.1	Iron fed	198
7.2	Iron + clioquinol	200
7.3	Iron + L-DOPA	202
7.4	Clioquinol	204
7.5	L-DOPA	206
7.6	Control animal	208
7.7	Discussion	210
7.7.1	External calibration	210
7.7.2	Biological significance	211
7.8	Conclusions	213
8	Application of elemental bio-imaging to 6-hydroxydopamine lesioned rodents.....	214
8.1	6-OHDA lesion	214
8.2	Control animals	217
8.3	Conclusions	218
9	Conclusions and recommendations.....	219
	References	222
	Appendix A – Excel VBA Macro v1	241
	Appendix B – Excel VBA Macro v2	246
	Appendix C – Excel VBA Macro v3	253
	Appendix D – Excel VBA Macro v4.....	258

List of figures

Figure 1.1: Macro view of two $\beta\beta\alpha$ zinc finger proteins bound to a DNA molecule. The DNA is shown as a white/light blue space-filling model. DNA binding domains of the zinc fingers are coloured red. From [17].	5
Figure 1.2: Structural diagram of the zinc centre of Zn finger proteins. Two histidine and two cysteine amino acid residues bind the central Zn^{2+} ion. Additional structural features include a single α -helix and two β -sheets [17].	6
Figure 1.3: Sources of metal species and areas of interest in metallomics. Trace elements and metal species are sourced from 4 major areas. Environmental and industrial exposure introduces numerous toxins, whilst plant and animal biochemistry, as well as endogenous processes involve essential elements. From [22].	7
Figure 1.4: Schematic model of the relationship between 'omic' sciences. 'M' represents a metal species. This figure highlights how trace elements are involved in numerous cellular and interstitial processes. From [5].	8
Figure 1.5: Simplified primary structure of the N-terminus of HSA. Red = aspartic acid (Asp), blue = alanine (Ala), grey = histidine (His) and green = lysine (Lys)	11
Figure 1.6: Cutaneous melanoma. From [60].	13
Figure 1.7: Basic structure of melanin polymer showing regions responsible for electron transfer, photon absorption through conjugated semiquinones and cation binding [65]. Carbonyl, amine and quinol groups allow for the formation of multi-dentate ligands with di- and tri-valent metal species.	14
Figure 1.8: Sentinel lymph nodes are the primary site of lymphatic draining in relation to a tumour [79].	15
Figure 1.9: H&E stain of superficial spreading melanoma, characterised by the 'dusty' pink cytoplasm seen in the bottom of the image. From [86]	17
Figure 1.10: H&E stain of lentigo melanoma. LN shows a more distinct boundary between malignant cells and healthy tissue [86].	18
Figure 1.11: S100 protein-containing cells labelled red in a sentinel lymph node [60].	19
Figure 1.12: Gaussian distribution of the absorbance intensity ratio of cytosine and guanine to total versus thymine to amide II in melanoma analysed by FTIR spectroscopy [90].	20
Figure 1.13: SIMS images of melanoma cells cultured in a mouse lung. A = CN^- , B = P^- and C = I^- . The bottom three images are overlays, where green represents P^- , red represents CN^- and purple represents I^- . Cyanide images are indicative of C and N containing molecules, including proteins and melanin, whereas P is predominately indicative of nucleic acids. Iodine is representative of the marker iodobenzamide [94].	21
Figure 1.14: SIMS images of melanoma cell culture treated with $\text{Na}_2^{10}\text{B}_{12}\text{H}_{11}\text{SH}$;BSH. The image labelled IIE is the ion-induced electron image. Measurement of Na, K and the K/Na ratio ensured cellular structure remained intact after freeze-drying. The ^{10}B image indicates a greater distribution in the extracellular material, which was seen to change by increasing incubation times [95].	22
Figure 1.15: Timm's stain of adult rat brain. Areas highlighted contain significant amounts of free or loosely bound Zn^{2+} . N = neocortex, H = hippocampus and B = basal ganglia [109].	26
Figure 1.16: SLC39 regulated cellular uptake of Zn. hZip 1 2 and 4 control intake of Zn, whilst an unidentified SLC39 protein is thought to regulate movement of Zn in and out of organelles. From [111].	28

Figure 1.17: Flowchart depicting the formation of the reactive oxygen species. Adapted from [99]. Dissolved diatomic oxygen (O_2) is reduced to superoxide (O_2^-) by redox active metals (Fe, Cu, Mn, Cd, Hg, Pb). The reactive superoxide anion is converted to H_2O_2 by enzymes from the superoxide dismutase group by another redox reaction with a metal ion [113]. Conversion of H_2O_2 to ROS and OH^- ions controlled by the Fenton reaction. In neurological disease a possible excess of redox metals is sourced from metalloprotein aggregates, like Fe: α -synuclein in PD and Cu/Zn:A β in AD.	29
Figure 1.18: Proposed mechanism of metal-mediated A β toxicity in AD [109]. 1) Fe and Cu increase with age, as do levels of APP and A β . 2) Fe and Cu:A β complexes catalyse the formation of H_2O_2 from molecular oxygen. H_2O_2 produced at this step does not necessarily cause ROS to form 3) H_2O_2 then oxidises the metal:A β complexes which are released from the cell membrane as cross linked oligomers. 4) Free Zn^{2+} in the synapse stimulates the precipitation of A β oligomers, histologically visible as plaques rich in Zn, Cu and Fe. 5) Microglia (neurological immune cells) respond to A β plaque deposition by releasing more H_2O_2 , which in turn continues to process in step 3. 6) Membrane-permeable H_2O_2 enters the cell, reacting with redox active metals according to the Fenton reaction, forming ROS that cause oxidative damage.	33
Figure 1.19: Increasing incidence of PD according to age and sex. From [129].	37
Figure 1.20: Top: 1-methyl 4-phenyl 1,2,3,6-tetrahydropyridine (MPTP). Bottom: 1-methyl-4-phenylpyridinium (MPP+).	38
Figure 1.21: Lewy bodies (indicated by arrows) stained with an anti- α -synuclein antibody. From [140].	39
Figure 1.22: Transport and storage of Fe in pigmented neurons found in the SN. From [140]	41
Figure 1.23: Structure of clioquinol, the first MPAC to be studied.	43
Figure 1.24: Mechanism of MPTP neurotoxicity showing involvement of Fe^{2+} ions. DAT = dopamine transporter. From [165].	44
Figure 1.25: Mechanism of 6-OHDA induced cell death, showing involvement of Fe^{2+} . From [165].	45
Figure 1.26: Tyrosine hydroxylase activity in a lesioned and unlesioned adult rat. The lesioned animal was injected with 6-OHDA during the neonatal development stage. TH is an enzyme that converts tyrosine to dihydroxyphenylalanine (L-DOPA) and is an essential part of the dopamine pathway. Decreased TH activity is indicative of dopaminergic neuron loss [166].	46
Figure 1.27: Number of published biological applications of LA-ICP-MS. Source ISI Web of Knowledge, keywords 'laser ablation', 'ICP-MS' and 'biology' (* to October 2008).	47
Figure 1.28: Prototype Sciex ICP-MS, circa 1981. From [171].	48
Figure 1.29: Schematic representation of analyte progression during plasma residence.	49
Figure 1.30: Diagram of ICP torch. Reproduced with permission from Agilent Technologies.	50
Figure 1.31: Degrees of ionisation for the entire periodic table at $T = 7500\text{ K}$ and $n_e = 1 \times 10^{15}\text{ cm}^{-3}$. Values in parentheses represent doubly charged (M^{++}) ions. * M^{++} formation not reported. From [176].	52
Figure 1.32: Ion focusing of three particles with different kinetic energies. E1 = Einzel lens 1 (-30 V), P = front and back stop plates (-14 V), B = Bessel box barrel (4 V) and S2 = stop plate 2 (-9 V). Adapted from [179].	54
Figure 1.33: Schematic representation of a quadrupole mass analyser, taken from [181]. Changing the applied DC and RF potential ($U-V\cos\omega t$) to each pair of metal rods to set values allows for specific m/z values to pass through with a stable trajectory.	55
Figure 1.34: Block diagram of a LA-ICP-MS unit. Adapted from [192].	63

Figure 1.35: Energy level diagram of Cr ³⁺ ions in a ruby laser. From [194].	64
Figure 1.36: Energy level diagram of Nd:YAG laser. From [194].	65
Figure 1.37: Energy profile of the upper and lower energy levels of an excimer laser. From [194].	66
Figure 1.38: White light interferometric light microscopic images of laser ablation crater in glass from 40 shots with 193 and 213 nm laser (a) and b)), with corresponding depth profiles (c) and d)) [192].	67
Figure 1.39: Repeated laser shots and their effect on crater profile. From [200].	68
Figure 1.40: Distance of crater from the outlet of specially design ablation cell. Narrower, more intense peaks are achieved closer to the cell outlet [202].	69
Figure 1.41: Experimental set-up for in-torch laser ablation using a Perkin-Elmer ELAN ICP-MS [204].	70
Figure 1.42: Cell design described by Feldmann <i>et al</i> [206]. 1 = PTFE insert, 2 = quartz window, 3 = gas inlet, 4 = gas outlet, 5 = membrane holder and 6 = rotary knob.	71
Figure 1.43: Single line scan of ⁶³ Cu in LGC7112 pig liver paste with and without ¹³ C normalisation. RSDs for the raw and normalised signal were 12% and 5.2%, respectively [207].	74
Figure 1.44: 40 µm diameter craters ablated in Ar (left) and He (right) atmospheres [226].	76
Figure 1.45: Typical workflow for imaging by LA-ICP-MS.	78
Figure 1.46: Quantitative images of a) Zn and b) Cu in human hippocampus sections. Taken from [242].	81
Figure 1.47: Comparison of light micrograph and Zn, Cu and Pb regional distribution within the posterior insular region of a human brain [243].	82
Figure 1.48: Parallel sections of human brain 20 µm apart. The concentration of Cu and Zn and raw signal of ¹³ C was measured in areas marked a), b) and c) and compared for reproducibility studies [244].	83
Figure 1.49: a) Peripheral benzodiazepine receptor, b) A ₁ adenosine receptor ligand, c) Cu and d) Zn distribution within tumour containing brain tissue. Tumour is marked by the white arrows [245].	84
Figure 1.50: Image of ⁸⁸ Sr/ ⁴⁸ Ca ratio in fish scale. Resolution is approximately 30 µm [220].	85
Figure 1.51: ¹³ C, ³² S, ³¹ P, ⁵⁶ Fe, ⁶³ Cu and ⁶⁶ Zn images of sections taken from a Sprague-Dawley rat. DG = dentate gyrus, SN = substantia nigra, MGN = medial geniculate nucleus, SC = superior colliculus and PGA = periaqueductal grey [247].	86
Figure 1.52: ⁶³ Cu image of implanted tumour in male F344 Fisher rat brain. Laser spot size 50 µm [248].	86
Figure 1.53: a) Cu, b) Zn and c) Pt distribution in <i>cis</i> -platin treated mice kidneys. Laser spot size 50 µm [241].	87
Figure 1.54: Photograph (top) and ¹⁵³ Eu image (bottom) of monoclonal Aβ antibody and Eu-labelled streptavidin protein in TASTPM transgenic mouse brain [250].	88
Figure 2.1: Agilent 7500ce ICP-MS	96
Figure 2.2: New Wave UP213 laser ablation unit	98
Figure 2.3: Schematic representation of imaging experiments	102
Figure 2.4: Data processing workflow	103
Figure 2.5: x-y-z representation of imaging experiments	105
Figure 2.6: Workflow for production of matrix-matched tissue standards. SN = solution nebulisation.	106
Figure 2.7: Power program for microwave digestion of tissue standard	107
Figure 2.8: Signal profile for external calibration experiments	109
Figure 2.9: Two-dimensional layout of collated external calibration data.	110

Figure 2.10: Diagram showing position of dried droplets on a microscope slide. Each colour represents the extracted ROI, with the light blue areas representing the ROI used for background subtraction.	113
Figure 2.11: Diagram showing position of dried droplets on tissue section. Each colour represents the extracted ROI, with the light blue areas representing the ROI used for tissue background subtraction.	114
Figure 2.12: Dorsal view 6-OHDA lesioned Sprague-Dawley rat brains, produced by the Dept. of Pharmacology and Physiology, Karolinska Institutet, Stockholm, Sweden.....	116
Figure 2.13: Substantia nigra (left) and striatal (right) sections from 6-OHDA lesioned Sprague-Dawley rats. The lesion was made in the right hemisphere.....	116
Figure 2.14: Nissl stained section of 6-OHDA lesioned animal from MHRIV. Lesion is in the right hemisphere.....	118
Figure 2.15: Rodent brain at bregma – 4.80 mm. 3rd V PAG = dorsal third ventricle and periaqueductal grey, A-Hip = amygdalohippocampal area, APT = anterior pretectal nucleus, DG = dentate gyrus, DLG = dorsal part of the lateral geniculate nucleus, MM = medial mamillary nucleus, pc = posterior commissure, SN = substantia nigra (pars compacta and reticulata), Thal = thalamus. Adapted from [266, 269].	120
Figure 3.1: Spot ablation dimensions for experiments using 40 μm laser spot size.....	122
Figure 3.2: Light micrograph of tissue post ablation.	123
Figure 3.3: Spot ablation dimensions for experiments using square 65 μm laser spot size. .	124
Figure 3.4: ^{63}Cu image of 6-OHDA lesioned Sprague-Dawley rat brain at the level of the SN using 40 μm spot. Complete laser parameters are given in Table 3.1.	125
Figure 3.5: ^{66}Zn image of 6-OHDA lesioned Sprague-Dawley rat brain at the level of the SN using 40 μm spot. Complete laser parameters are given in Table 3.1.	125
Figure 3.6: ^{31}P image of 6-OHDA lesioned Sprague-Dawley rat brain at the level of the SN using square 65 μm spot. The white oval highlights a possible area of cell damage from the lesioning procedure. Complete laser parameters are given in Table 3.2.	126
Figure 3.7: ^{57}Fe image of 6-OHDA lesioned Sprague-Dawley rat brain at the level of the SN using square 65 μm spot. The arrow shows the direction of syringe used to inject 6-OHDA. The white oval highlights a possible area of cell damage from the lesioning procedure. Complete laser parameters are given in Table 3.2.	127
Figure 3.8: ^{27}Al , ^{43}Ca , ^{55}Mn , ^{63}Cu , ^{24}Mg , and ^{66}Zn images of 6-OHDA lesioned Sprague-Dawley rat brain at the level of the SN using square 65 μm spot. Complete laser parameters are given in Table 3.2.	128
Figure 3.9: ^{31}P image of 6-OHDA lesioned Sprague-Dawley rat brain at the level of the striatum (denoted by the white circles) using square 65 μm spot. Black oval = anterior commissure. Complete laser parameters are given in Table 3.2.	129
Figure 3.10: ^{66}Zn and ^{63}Cu images of 6-OHDA lesioned Sprague-Dawley rat brain at the level of the striatum using square 65 μm spot. Complete laser parameters are given in Table 3.2.	130
Figure 3.11: Schematic representation of line ablation experiments using a 40 μm laser spot.	131
Figure 3.12: ^{31}P image of 6-OHDA lesioned Sprague-Dawley rat brain at the level of the striatum using square 65 μm spot. Complete laser parameters are given in Table 3.3.	132
Figure 3.13: Signal vs. time plot of extracted segment from ^{66}Zn image shown in Figure 3.5.	134
Figure 3.14: Schematic representation of data extraction procedure used for ENVI spot ablation images.	135

Figure 3.15: ^{31}P image of 6-OHDA lesioned Sprague-Dawley rat brain at the level of the SN using a $40\text{ }\mu\text{m}$ spot and 4 mL min^{-1} He collision gas. Complete laser parameters are given in Table 3.7.	137
Figure 3.16: Logarithmic signal vs. time plot of ^{31}P signal from a single line of ablation of rat brain tissue.	138
Figure 3.17: ^{56}Fe image of 6-OHDA lesioned Sprague-Dawley rat brain at the level of the SN using a $40\text{ }\mu\text{m}$ spot and 4 mL min^{-1} He collision gas. Complete laser parameters are given in Table 25.	138
Figure 3.18: ^{57}Fe image of 6-OHDA lesioned Sprague-Dawley rat brain at the level of the SN using a $40\text{ }\mu\text{m}$ spot and 4 mL min^{-1} He collision gas. Complete laser parameters are given in Table 25.	139
Figure 3.19: ^{66}Zn image of 6-OHDA lesioned Sprague-Dawley rat brain at the level of the SN using a $40\text{ }\mu\text{m}$ spot and 4 mL min^{-1} He collision gas. Complete laser parameters are given in Table 25.	140
Figure 3.20: Schematic representation of a single 1-second mass scan cycle relative to a 1 second laser pulse.	143
Figure 3.21: ^{27}Al and ^{208}Pb images of 6-OHDA lesioned Sprague-Dawley rat brain at the level of the SN using $40\text{ }\mu\text{m}$ spot. Experimental parameters from Table 3.1.	144
Figure 3.22: Simplified phase diagram of three isotopes.	145
Figure 3.23: ^{51}V image of 6-OHDA lesioned Sprague-Dawley rat brain at the level of the SN using square $65\text{ }\mu\text{m}$ spot. Complete laser parameters are given in Table 3.2.	145
Figure 3.24: Total power output and surface power density profile for New Wave UP213 Nd:YAG laser.	147
Figure 3.25: Effect of laser power on ^7Li , ^{182}W and ^{238}U response in NIST 612 glass, normalised to ^{28}Si . Laser parameters: spot size = $100\text{ }\mu\text{m}$, frequency = 20 Hz , dwell time = 2 s	147
Figure 3.26: Effect of laser power on ^{47}Ti and ^{66}Zn and response in NIST 612 glass, normalised to ^{28}Si . Laser parameters: spot size = $100\text{ }\mu\text{m}$, frequency = 20 Hz , dwell time = 2 s	148
Figure 3.27: Combined logarithmic plot of laser fluence (red axis) and NIST 612 glass ablation response (blue axis) vs. laser power output.	148
Figure 3.28: Effect of increasing surface energy density on crater shape in a $30\text{ }\mu\text{m}$ thick tissue matrix. Laser parameter: spot size = $55\text{ }\mu\text{m}$, frequency = 20 Hz , dwell time = 1 s	149
Figure 3.29: Effect of increasing laser power in tissue ablation on integrated ^{13}C response in three separate experiments. Laser parameter: spot size = $55\text{ }\mu\text{m}$, frequency = 20 Hz , dwell time = 1 s	150
Figure 3.30: Effect of increasing surface energy density on line ablation in a $30\text{ }\mu\text{m}$ thick tissue matrix. Laser parameter: spot size = $55\text{ }\mu\text{m}$, frequency = 20 Hz , scan speed = $55\text{ }\mu\text{m s}^{-1}$, line length approximately $500\text{ }\mu\text{m}$	151
Figure 3.31: Response of two major (% w/w) components (^{28}Si and ^{44}Ca) of NIST glass when laser power output was increased.	152
Figure 3.32: Effect of laser power on ^7Li , ^{182}W and ^{238}U response in NIST 612 glass without normalisation to an internal standard. Laser parameters: spot size = $100\text{ }\mu\text{m}$, frequency = 20 Hz , dwell time = 2 s	153
Figure 3.33: Effect of laser power on ^{47}Ti and ^{66}Zn and response in NIST 612 glass without normalisation to an internal standard. Laser parameters: spot size = $100\text{ }\mu\text{m}$, frequency = 20 Hz , dwell time = 2 s	153
Figure 3.34: Effect of signal normalisation on quality of ^{56}Fe image from a 6-OHDA lesioned mouse brain. a) Pre- and b) post normalisation to ^{13}C . Laser parameters: spot size = 30	

μm , scan speed = $30 \mu\text{m s}^{-1}$, line spacing = $30 \mu\text{m}$, frequency = 20 Hz, laser power output = 35%.	154
Figure 3.35: The effect of ^{13}C signal normalisation on high m/z 56 background levels. Signal ratio = green axis.	155
Figure 3.36: ^{56}Fe image of the same MHRIV 6-OHDA lesioned mouse brain section a) before and b) after background $^{40}\text{Ar}^{16}\text{O}^+$ removal. Circled areas in image b) include the lower dentate gyrus (1), periaqueductal grey (2) and the right SN (3), where contrast is improved after background subtraction. Laser parameters: spot size = $30 \mu\text{m}$, scan speed = $30 \mu\text{m s}^{-1}$, line spacing = $30 \mu\text{m}$, frequency = 20 Hz, laser power output = 35%.	156
Figure 3.37: ^{13}C signal of 1.2 L min^{-1} bottled welding grade Ar carrier gas.	157
Figure 3.38: ^{13}C signal of 1.2 L min^{-1} high purity Ar carrier gas from liquid Ar source.	157
Figure 3.39: Mass spectra of welding grade Ar gas blank	158
Figure 3.40: Mass spectra of Ar sourced from liquid dewar	159
Figure 3.42: a) and c) ^{60}Ni images. b) and d) Photographs of corresponding tissue sections.	160
Figure 3.43: ^{60}Ni signal for line 112 (of a total 132 lines) of image from striatal section of Sprague-Dawley rat. Laser parameters: spot size = $65 \mu\text{m}^2$, grid spacing = $65 \mu\text{m}$, frequency = 20 Hz, dwell time = 1 s, intersite pause = 3 s, laser power output = 50%.	160
Figure 3.44: Peak shape and methods of integration.	161
Figure 4.1: Droplet position and corresponding m/z 63 and 65 images. Droplet contents are summarised in Table 2.11. Red X indicates that no signal was obtained from potentially interfering polyatomics. Experimental parameters are given in Table 4.1.	166
Figure 4.2: Droplet position and corresponding m/z 56 and 57 images. Droplet contents are summarised in Table 2.11. Red X indicates that no signal was obtained from potentially interfering polyatomics. Experimental parameters are given in Table 4.1.	167
Figure 4.3: Droplet position and corresponding m/z 63 and 65 images from ablation of droplets on tissue. Droplet contents are summarised in Table 2.12. Experimental parameters are given in Table 4.2.	169
Figure 4.4: Droplet position and corresponding m/z 56 and 57 images from ablation of droplets on tissue. Droplet contents are summarised in Table 2.12. Experimental parameters are given in Table 4.2.	170
Figure 4.5: Droplet position and corresponding m/z 64 and 66 images from ablation of droplets on tissue. Droplet contents are summarised in Table 2.12. Experimental parameters are given in Table 4.2.	171
Figure 4.6: Droplet position and corresponding m/z 55 image from ablation of droplets on tissue. Droplet contents are summarised in Table 2.12. Experimental parameters are given in Table 4.2.	172
Figure 5.1: 10 x light micrograph of malignant melanoma showing large atypical cells.	178
Figure 5.2: ^{31}P , ^{34}S , ^{63}Cu and ^{66}Zn images of a healthy lymph node.	179
Figure 5.3: Comparative images of sentinel lymph node impregnated with melanoma. (a) Photograph of slice before elemental imaging, (b) H + E stain, (c) ^{31}P image (units counts per second), (d) $^{31}\text{P}^+$, (e) $^{31}\text{P}^+ / ^{34}\text{S}^+$ and (f) $^{31}\text{P}^+ / ^{66}\text{Zn}^+$	180
Figure 5.4: Lymph nodes impregnated with melanoma. (a) H + E stain, (b) ^{31}P image, (c) $^{31}\text{P} / ^{34}\text{S}$ and (e) $^{31}\text{P} / ^{66}\text{Zn}$	181
Figure 5.5: Lymph node impregnated with melanoma. (a) H + E stain, (b) ^{31}P image, (c) $^{31}\text{P} / ^{34}\text{S}$ and (d) $^{31}\text{P} / ^{66}\text{Zn}$	182
Figure 5.6: Lymph node impregnated with melanoma. (a) H + E stain, (b) ^{31}P image, (c) $^{31}\text{P} / ^{34}\text{S}$ and (d) $^{31}\text{P} / ^{66}\text{Zn}$	183

Figure 5.7: Lymph nodes impregnated with melanoma. (a) H + E stain, (b) ^{31}P image, (c) $^{31}\text{P}/^{34}\text{S}$ and (d) $^{31}\text{P}/^{66}\text{Zn}$	184
Figure 5.8: Overlaid ^{31}P image with 4 x light micrograph of lymph node impregnated with malignant melanoma cells showing boundary between normal and metastatic cells...	185
Figure 5.9: Overlaid ^{31}P image and light micrograph (4 x and 10 x) of lymph node showing boundary of normal and metastatic melanoma cells.	185
Figure 5.10: ^{31}P image and light micrograph of small node with approximately 1 mm diameter tumour infiltration.	186
Figure 5.11: 3-dimensional surface view of ^{31}P signal in lymph node partially infiltrated by malignant melanoma. 2-dimensional images are shown in Figure 5.3.	187
Figure 5.12: 3D ^{31}P surface maps of lymph node impregnated with melanoma cells (Figure 5.3), rotated in 45 degree increments.	187
Figure 5.13: 3D ^{31}P surface maps of lymph node impregnated with melanoma cells (Figure 5.4), rotated in 45 degree increments.	188
Figure 5.14: 3D ^{31}P surface maps of lymph node impregnated with melanoma cells (Figure 5.5), rotated in 45 degree increments.	188
Figure 5.15: 3D ^{31}P surface maps of lymph node impregnated with melanoma cells (Figure 5.7), rotated in 45 degree increments.	189
Figure 6.1: Calibration curves for each aqueous standard used in solution nebulisation ICP-MS experiments	192
Figure 6.2: Percentage recoveries of each spiked element.	195
Figure 7.1: Regions of interest for data extraction containing the SN (marked in red).	198
Figure 7.2: Region of interest for data extraction containing all areas of the midbrain ventral to the dorsal 3rd ventricle (marked in blue).	198
Figure 7.3: ^{56}Fe image from Fe fed animal	199
Figure 7.4: ^{63}Cu , ^{55}Mn , ^{66}Zn and ^{31}P images from Fe-fed animal.....	199
Figure 7.5: ^{56}Fe image from Fe-fed, CQ treated animal	201
Figure 7.6: ^{63}Cu , ^{55}Mn , ^{66}Zn and ^{31}P images from Fe-fed, CQ treated animal	201
Figure 7.7: ^{56}Fe image from Fe-fed, L-DOPA treated animal.	203
Figure 7.8: ^{63}Cu , ^{55}Mn , ^{66}Zn and ^{31}P images from Fe-fed, L-DOPA treated animal.	203
Figure 7.9: ^{56}Fe image from CQ treated animal.	205
Figure 7.10: ^{63}Cu , ^{55}Mn , ^{66}Zn and ^{31}P images from CQ treated animal.....	205
Figure 7.11: ^{56}Fe image from L-DOPA treated animal.	207
Figure 7.12: ^{63}Cu , ^{55}Mn , ^{66}Zn and ^{31}P images from L-DOPA treated animal.....	207
Figure 7.13: ^{56}Fe image from control animal.	209
Figure 7.14: ^{63}Cu , ^{55}Mn , ^{66}Zn and ^{31}P images from control treated animal.....	209
Figure 7.15: a) Tyrosine hydroxylase immunohistochemical stain, b) ^{56}Fe and c) overlaid images from control animal. The black spot on the lower right of a) is artefact.....	211
Figure 8.1: ^{56}Fe image of 6-OHDA lesioned mouse brain at the level of the SN. The white arrow shows the needle track. The circle indicates the SN.	215
Figure 8.2: ^{63}Cu , ^{55}Mn and ^{66}Zn images of 6-OHDA lesioned animal.	216
Figure 8.3: 12 μm resolution ^{56}Fe and ^{66}Zn images of 6-OHDA lesioned animal. The signal due to high Fe concentrations surrounding the needle track was set to zero for image clarity.	217
Figure 8.4: Three-dimensional surface view of ^{56}Fe 12 μm resolution image.	217
Figure 9.1: FTIR images of 6-OHDA lesioned rats. SN section (left) and striatal section (right). Reproduced with permission of Fiona Burger.	220

List of tables

Table 1.1: Essential elements found in the human body. Adapted from [1].	2
Table 1.2: Typical trace element-containing enzymes. From [5].	3
Table 1.3: Organisational framework of neurological disorders associated with metals. Originally proposed by Strozyk and Bush in [99].	23
Table 1.4: Causes of Parkinsonism. Adapted from [99].	38
Table 1.5: Common polyatomic interferences arising from biological matrices.	58
Table 1.6: Comparison of background signals measured by LA and solution nebulisation ICP-MS. Adapted from [222]. * blank 1% HNO ₃ solution.	75
Table 1.7: Selected imaging applications	92
Table 2.1: Typical operational parameters for Agilent 7500 ce ICP-MS. Note that Octopole Reaction System settings are only used when reaction mode is on.	99
Table 2.2: Operational conditions for Varian UltraMass 700 ICP-MS in solution mode.	99
Table 2.3: Concentrations of trace elements in NIST 612 glass. * <i>certified value</i> .	100
Table 2.4: Sensitivity targets for LA-ICP-MS tuning by NIST 612 glass. Laser parameters: spot size = 100 μm , scan speed = 5 $\mu\text{m s}^{-1}$, frequency = 20 Hz, laser power output = 100%, energy density = 15 mJ cm^{-2}	100
Table 2.5: Typical operational parameters for Agilent 7500 ce ICP-MS when used with the New Wave UP123 laser ablation unit. Note that the ORS was disabled.	101
Table 2.6: Arrangement of data for BIL file format	103
Table 2.7: Arrangement of data for BSQ file format	104
Table 2.8: Approximate amounts added to each tissue standard	106
Table 2.9: Concentrations of prepared aqueous standard for solution ICP-MS external calibration	108
Table 2.10: Typical operation parameters for LA-ICP-MS interference experiments.	112
Table 2.11: Composition of 5 test solutions for glass interference experiments. All solutions were made to volume using 1% HNO ₃ .	112
Table 2.12: Composition of 4 test solutions for tissue interference experiments. All solutions were made to volume using 1% HNO ₃ .	114
Table 3.1: Experimental parameters for Figure 3.4 and Figure 3.5.	126
Table 3.2: Experimental parameters used for Figure 3.6 to Figure 3.10.	131
Table 3.3: Experimental parameters for Figure 3.12	133
Table 3.4: Arrangement of data for image generation using SigmaPlot, where n = total number of data points per line and m = number of lines.	134
Table 3.5: Parameters altered from typical no gas LA-ICP-MS tune for use with 4 mL min^{-1} He gas.	136
Table 3.6: Analyte ions monitored and potential expected polyatomic interferences.	136
Table 3.7: Experimental parameters for Figure 3.15 to Figure 3.19	140
Table 4.1: Experimental parameters for Figure 4.1 and Figure 4.2	165
Table 4.2: Experimental parameters for Figure 4.3 to Figure 4.6	165
Table 4.3: Isotopic abundance patterns for selected isotopic elements.	168
Table 4.4: Comprehensive list of polyatomic interferences on the major isotopes of Mn, Fe, Cu and Zn possible in biological matrices. Adapted from [284].	168
Table 4.5: Expected and recorded isotopic abundance ratios for Fe, Cu and Zn.	172
Table 5.1: Experimental parameters for all lymph node images.	177

Table 6.1: Errors in slope and intercept, with detection limits and background equivalent concentrations calculated from linear regression analysis of solution nebulisation ICP-MS standards.	193
Table 6.2: Approximate and actual concentration of spiked tissue standard digests	194
Table 7.1: LA-ICP-MS operational parameters.....	197
Table 7.2: Statistical error in the slope and intercept for each measured quantified isotope.	200
Table 7.3: Quantitative data extracted from specified regions of interest from Fe-fed animal.	200
Table 7.4: Statistical error in the slope and intercept for each measured quantified isotope.	202
Table 7.5: Quantitative data extracted from specified regions of interest from Fe-fed, CQ treated animal.....	202
Table 7.6: Statistical error in the slope and intercept for each measured quantified isotope.	204
Table 7.7: Quantitative data extracted from specified regions of interest from Fe-fed, L-DOPA treated animal.....	204
Table 7.8: Statistical error in the slope and intercept for each measured quantified isotope.	206
Table 7.9: Quantitative data extracted from specified regions of interest from CQ treated animal.	206
Table 7.10: Statistical error in the slope and intercept for each measured quantified isotope.	208
Table 7.11: Quantitative data extracted from specified regions of interest from L-DOPA treated animal.....	208
Table 7.12: Statistical error in the slope and intercept for each measured quantified isotope.	210
Table 7.13: Quantitative data extracted from specified regions of interest from control animal.	210
Table 7.14: Comparison of solution nebulisation ICP-MS analysis of SN from Wistar rats and LA-ICP-MS analysis of C57Bl/6 mice.	212
Table 7.15: Fe concentration in each treatment group.	213
Table 8.1: Comparison of Fe concentrations within the SN by LA-ICP-MS and SN-ICP-MS....	218

List of publications

D. Hare, B. Reedy, R. Grimm, S. Wilkins, I. Volitakis, J. George, R. Cherny, A. Bush, D. Finkelstein, P. Doble. *Quantitative elemental bio-imaging of Mn, Fe, Cu and Zn in 6-hydroxydopamine Parkinsonism mouse models*. Metallomics, DOI:10.1039/B816188G

D. Hare, F. Burger, C. Austin, F. Fryer, R. Grimm, B. Reedy, R. Scolyer, J Thompson, P. Doble. *Elemental bio-imaging of melanoma in lymph node biopsies*. The Analyst, DOI:10.1039/B812745J

D. Hare, B. Reedy, F. Fryer, R. Grimm, J. George, S. Wilkins, D. Finkelstein, P. Doble. *Elemental bio-imaging: in situ analysis of trace elements in tissue sections*. Invited oral presentation at the Asia-Pacific Winter Plasma Conference on Plasma Spectrochemistry, Tsukuba, Japan, November 2008.

D. Hare, B. Reedy, M. Dawson, F. Fryer, R. Svenningsson, R. Grimm, P.E. Andren, P. Doble. *Metal-imaging mass spectrometry (MIMS): A new imaging mass spectrometry technology to determine the distribution of metal ions in tissue samples*. Oral presentation at the Joint 4th Asia Oceania Human Proteome Organization and 2nd Pacific Rim International Congress on Protein Science, Cairns, Australia, June 2008.

D. Hare, C. Austin, D. Bishop, A. Beavis, B. Reedy, M. Dawson, F. Fryer, R. Svenningsson, X. Zhang, R. Grimm, P. Andren, P. Doble. *Metal Imaging Mass Spectrometry: laser ablation-inductively coupled plasma-mass spectrometry imaging of 6-ohda induced Parkinson's disease and melanoma in lymphatic tissue*. Awarded 2nd place poster prize at the Royal Australian Chemical Institute Research and Development Conference, Adelaide, December 2007.

D. Hare, B. Reedy, M. Dawson, C. Austin, F. Fryer, R. Svenningsson, X. Zhang, R. Grimm, P. Andren, P. Doble. *Metal-imaging Mass Spectrometry (MIMS): a new imaging mass spectrometry technology to determine the distribution of metal ions in tissue samples*. Oral presentation at the International Symposium on Metallomics, Nagoya, Japan, November 2007.

D. Hare, B. Reedy, M. Dawson, F. Fryer, R. Svenningsson, R. Grimm, P.E. Andren, P. Doble. *Metal-imaging mass spectrometry (MIMS): A new imaging mass spectrometry technology to determine the distribution of metal ions in tissue samples.* Poster presented at the Human Proteome Organization 6th Annual World Congress, Seoul, South Korea, October 2007.

D. Hare, B. Reedy, M. Dawson, F. Fryer, R. Grimm, P. Andren, P. Doble. *Trace element imaging of 6-OHDA induced Parkinson's disease in rat brains using laser ablation ICP-MS.* Poster presentation at the European Winter Plasma Conference on Plasma Spectrochemistry, Taormina, Sicily, Italy, March 2007.

D. Hare, P. Doble. *Metal Imaging Mass Spectrometry: In situ analysis of trace elements in neurological tissue using laser ablation ICP-MS.* Oral presentation at the Australian and New Zealand Society for Mass Spectrometry Conference, Christchurch, New Zealand, January 2007.

Abstract

Elemental bio-imaging is a new application of laser ablation – inductively coupled plasma – mass spectrometry (LA-ICP-MS) that determines *in situ* trace element concentrations in thin sections of biological tissues. This project developed a LA-ICP-MS method for creating colour images of the regional distribution of both metals and non-metals in a variety of biological samples.

The developed method was capable of producing images with a lateral resolution as low as 30 μm . This was achieved using a 30 μm laser spot that was rastered across the sample at a rate of 30 $\mu\text{m s}^{-1}$. It was found that a laser fluence of 0.22-0.28 J cm^{-2} was best suited for soft tissue sections with minimal particle redeposition and fracturing of the surrounding sample. Evaluation of the octopole reaction system (ORS) fitted to the Agilent 7500 ce instrument found that the use of a collision gas for interference removal was inadvisable for imaging experiments. Experiments were carried out to determine the significance of potential polyatomic interferences in the ablation of tissue. It was found that the ‘dry’ nature of the plasma in LA-ICP-MS significantly reduced the occurrence of O and H based polyatomics, and the small sample load in each ablation reduced the effect of other matrix-based interferences on elements in the mg kg^{-1} concentration range.

Application of the method to sections of human lymph nodes impregnated with malignant melanoma found imaging of ^{31}P was able to accurately discern healthy cells from cancerous tissue. Measurement of the ratio between ^{31}P and other elements improved the contrast between the two types of cells. Three-dimensional models of imaged lymph nodes further improved the distinction between the melanoma cells and normal tissue.

A method was developed for producing matrix-matched tissue standards by homogenising chicken tissue with known amounts of added elemental standards. Digestion of the tissue standards was performed and analysis by solution nebulisation ICP-MS confirmed the concentration of each added element. The standards were frozen and cut to the desired thickness for ablation and construction of multi-point calibration curves.

An Fe-fed mouse model for Parkinson's disease (PD) was used to demonstrate the characteristics of the technique. C57BL6 mice were fed a diet high in Fe during development and were treated with both clioquinol (CQ) and L-DOPA, both of which are thought to chelate Fe in the brain. Results showed a decrease in Fe in the treated animals within the region of the brain called the substantia nigra (SN), which is adversely affected in PD.

A 6-hydroxydopamine (6-OHDA) model for PD was also examined. 6-OHDA is directly injected into the rodent brain, stimulating the loss of cells within the SN. Imaging of sections taken from 6-OHDA lesioned animals showed a significant increase in Fe within the SN bilaterally when compared to control animals.

In summary, elemental bio-imaging is a new method that can be applied to tissue sections from many sources, including humans. The technique has the potential to assist biologists in identifying possible new biomarkers for disease, related specifically to trace elements.